

Object Reconstruction under Occlusion with Generative Priors and Contact-induced Constraints

Minghan Zhu^{1,2}, Zhiyi Wang², Qihang Sun², Maani Ghaffari², and Michael Posa¹

Abstract—Object geometry is key information for robot manipulation. Yet, object reconstruction is a challenging task because cameras only capture partial observations of objects, especially when occlusion occurs. In this paper, we leverage two extra sources of information to reduce the ambiguity of vision signals. First, generative models learn priors of the shapes of commonly seen objects, allowing us to make reasonable guesses of the unseen part of geometry. Second, contact information, which can be obtained from videos and physical interactions, provides sparse constraints on the boundary of the geometry. We combine the two sources of information through contact-guided 3D generation. The guidance formulation is inspired by drag-based editing in generative models. Experiments on synthetic and real-world data show that our approach improves the reconstruction compared to pure 3D generation and contact-based optimization. Project page: <https://contactgen3d.github.io/>

I. INTRODUCTION

Vision is the most informative perception modality, but visual observation only captures partial information of the observed environment. Obtaining the full state of the environment through vision thus becomes an ill-posed problem, posing a significant challenge on robotic systems, which typically rely on knowledge of the environmental states. Take object manipulation as an example, object geometry and pose are the essential input [1, 2], but it is not trivial to estimate them from vision, due to the self-occlusion and the occlusion by other objects in the environments and by the robot itself. This long-standing challenge steered some robotic research efforts to end-to-end approaches [3, 4], where policies and actions are generated directly from raw observations, but they still suffer from limited generalizability and interpretability.

We argue that the problem caused by partial observability in visual perception can be alleviated, thus building better models of the environment, if we go beyond the raw pixels and leverage other sources of information. For example, by learning priors of object geometry from large datasets, generative models can build a full object model from a single image, even under occlusion. Meanwhile, we can obtain knowledge of the contacts between an object and the environment from visual observations and physical interactions. Contacts can only happen on the boundary of the geometry, thus imposing constraints on the object shape. Interestingly, the information from data-based shape priors and contact-induced constraints is usually complementary, as the “inpainting” of unobserved geometry by the generative

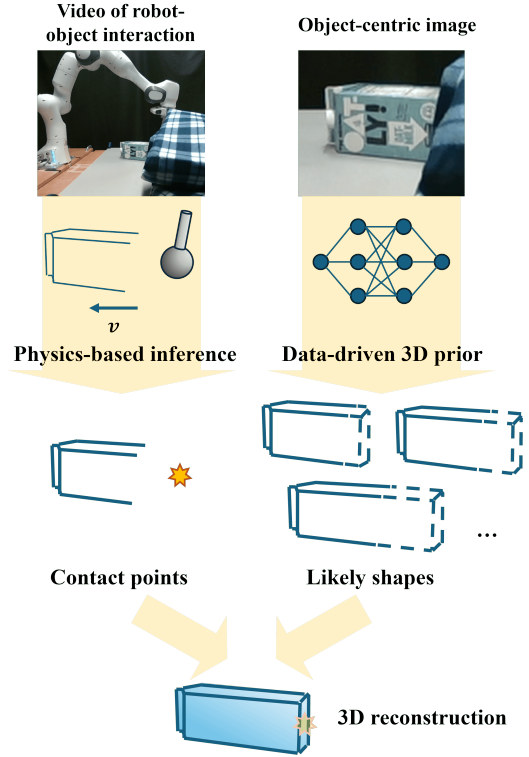


Fig. 1. This work develops a novel framework for 3D object reconstruction under occlusion by integrating data-driven 3D priors and physics-based contact information through guided generation. The two perspectives bring complementary insights that lead to high-quality and accurate 3D reconstruction.

model often has multiple solutions, and the sparse contact constraints can reduce the ambiguity.

In this paper, we tackle the problem of visual object reconstruction under occlusion by combining data-driven 3D priors and contact-induced constraints. A high-level overview is depicted in Figure 1. We use the paradigm of image-conditioned object generation to harness the powerful generative prior of object shapes. Specifically, we use a flow-matching 3D generative model dedicatedly designed to work with occluded 2D images, Amodal3R [5], as our base model for 3D generation. On the other hand, we model contact information as discrete points where the contacts occur. In our real-world experiments, we employ Vysics [6], a video-based framework that reconstructs object geometry and infers contact points, as the source of contact constraints.

We formulate the fusion as 3D generation with training-free contact guidance, where a contact-based energy function

¹University of Pennsylvania, Philadelphia, PA 19104 {minghz, posa}@seas.upenn.edu

²University of Michigan, Ann Arbor, MI 48109 {minghanz, jerrywzy, qhsun, maanigj}@umich.edu

is formulated based on the contact points and used to guide the inference of the flow-matching generative model. Specifically, we are inspired by drag-based editing in 2D image generation, and propose a drag-based 3D energy function for contact guidance. In this way, we can build the object geometry model from heavily occluded visual observations with high quality and good metric accuracy.

We summarize the core contributions of this work as follows:

- We propose an object reconstruction framework that incorporates data-driven generative priors and physics-driven contact constraints.
- We develop a guidance method for native 3D generation using a drag-based energy function.
- Our method achieves superior object reconstruction in synthetic and real-world data, highlighting the importance of synthesizing data-driven and physics-driven insights.

II. RELATED WORK

A. 3D Object Reconstruction

There are different paradigms that can be applied on the problem of object reconstruction. Object SLAM [7, 8] approaches rely on low-level tracking and shape-pose optimization, achieving good efficiency and generalizability, but lack robustness against visual signal degradation. In this paper, we mainly discuss object reconstruction by 3D generation, in which data-driven priors are used to build the complete geometry (and sometimes appearance) model of an object from one or a few images.

The development of 3D generative methods is largely inspired and supported by the progress in 2D image generative models. The denoising steps in 2D diffusion [9] can be interleaved with the regression [10, 11] or optimization [12] of 3D representations to reconstruct the 3D target. Moreover, multi-view image generation from a single image input [13, 14] provides strong 3D priors. Many works connect multi-view image generation with multi-view 3D reconstruction for 3D generation from a single image [15–17], or repurpose multi-view image generation capability for pixel-aligned 3D representation generation [18]. On the other hand, 3D generative priors can also be learned natively in 3D without relying on image generative priors. Earlier attempts [19, 20] are limited by the relatively small size of 3D datasets [21]. With larger datasets of 3D objects [22] being released, 3D generation models become much more powerful. Some [23–25] simply use implicit learnable tokens as the latent features for 3D generation, while others [26–28] use explicit 3D primitives in the latent space for better interpretability and controllability. We used a model based on explicit latent to formulate the contact-induced energy function more easily.

B. Occlusion-aware 3D Reconstruction

Despite the significant progress in 3D generation, most such models are trained to take an unoccluded image of the target as input, and their performance degrades significantly

when occlusion is present. To overcome this limitation, recent research has explored three main directions.

1) *Completing occluded areas in 2D*: In this paradigm, the occluded single-view image is first processed by a 2D amodal segmentation and completion model [29, 30] or an image inpainting model [31, 32] to recover the missing regions in the image space. The completed image is then provided to a 3D generative model for reconstruction. A representative example is SceneComplete [33], which integrates BrushNet [34] with InstantMesh [35]. CAST [36] employs a Masked Auto Encoder (MAE) [37] to complete the occluded area in the image latent space. However, the effectiveness of this pipeline is constrained by the quality of the 2D amodal completion or inpainting. It is also less straightforward to inject 3D guidance into the 2D generation process, which is important for our work.

2) *Shape completion from partial point clouds*: It is possible to condition 3D generative models on partial point clouds for 3D shape completion [19, 20, 38]. However, they require the input points to reside in the canonical object frame, which is usually unavailable in real-world use cases. They also typically require extra image, text, or category condition, as a partial point cloud alone may not carry enough information to recover the whole object. Specialized point cloud completion methods also exist [39–41], but they are trained either in a non-generative paradigm or on a relatively small dataset [21], limiting their performance and generalizability.

3) *Fine-tuning 3D generative models for occlusion*: Amodal3R [5] fine-tunes a native 3D generation framework, TRELLIS [26], with occlusion and visibility masks as additional input modalities, enabling robust handling of occlusions in single-view reconstruction.

C. Adding Controllability to Pretrained Generative Models

Here, we discuss three strategies for adding controllability to pretrained generative models. First, fine-tuning. Technologies like ControlNet [42] and adapters [43] allow fine-tuning a pretrained model to take in new modalities, usually spatial control signals such as edge maps and poses, without destroying the original representations. Second, training-free guidance, which does not require training the generative model with the condition. The guidance signal is formulated as an energy function to represent the compatibility between the generated states and the task-specific needs. In diffusion or flow-matching models, the goal is to find a delta step in each denoising iteration to steer the output to satisfy the task-specific needs. There has been extensive literature on diffusion guidance [44–46] and recently on flow-matching [47] as well. Third, we can also treat the controllable generation problem as an editing problem, where uncontrolled generation is first performed, and then we apply generative editing [48, 49] to make the outcome follow our specifications. In this paper, we incorporate the idea of editing in building a training-free guidance for contact-conditioned 3D generation.

D. Physics-based Reasoning in 3D Reconstruction

As discussed in the introduction, physics-based reasoning helps reduce the ambiguity in visual signals and build a physically plausible reconstruction. Many efforts assume the objects to be stable and static and use optimization to prevent penetration and unstable falling [50–52]. In [6, 53, 54], contact is analyzed in dynamic scenes to improve 3D reconstruction. Estimated physics properties may also be used to generate physically realistic videos [55, 56].

III. PRELIMINARIES

A. 3D Generation: TRELLIS and Amodal3R

Amodal3R [5] is a 3D generation model taking occluded images and masks as input. It is fine-tuned on TRELLIS [26], a flow-matching model capable of image-to-3D and text-to-3D generation. Our framework uses Amodal3R as the base model to provide 3D priors. Thus we will first introduce TRELLIS and Amodal3R briefly.

TRELLIS contains two stages for 3D generation: sparse structure generation and structured latent generation, which are in charge of the generation of the overall geometry and the local details and appearance, respectively. The sparse structure is a set of sparse voxels, representing the occupied geometry in resolution 64^3 in a unit cube. The structured latent is feature vectors attached to each occupied voxel, which can be decoded into 3D Gaussians or FlexiCube [57] representations of resolution 256^3 for mesh generation. The first stage output resolution is high enough for meaningful contact-induced guidance, thus we mainly focus on the first-stage guided generation in this paper, and keep the second stage as is. In the first stage, the latent space for sparse structure generation is a dense 3D voxel feature map, which is down-sampled to 16^3 resolution for memory efficiency. Amodal3R incorporates a visibility mask, which highlights the visible part of the object of interest, and an occlusion mask highlighting the occluder, as extra input. Please refer to the original papers for more details.

B. Vysics: Contact Estimation from Video

In our real-world experiments, contact information comes from Vysics [6], an optimization-based object tracking and 3D reconstruction framework that also infers contact points and associated contact force from a video of an object interacting with a robot and the environment, and uses the estimated contacts to assist in building the object model. In this paper, we use the estimated contact points from Vysics as the guiding signal for the 3D generation under occlusion.

C. Drag-based Generative Editing

The operation “dragging” originates from 2D image editing, where the goal is to move a point in the image to a different coordinate, while keeping the overall image semantically consistent and spatially reasonable. After the pioneering work DragGAN [58], the drag-based editing is also realized in diffusion models [48, 59]. On a high level, the drag-based editing in diffusion models can be done by adding noise to an image (as the reference) and denoising.

In the denoising process, a drag-based loss encourages the features around the target point to resemble the reference features around the source point, and a content-preservation loss encourages features everywhere else to be consistent with the reference. We will build our guidance in a similar drag-based formulation.

IV. METHOD

A. Problem Formulation

We formulate the fusion of data-driven 3D priors and sparse contact point data for object reconstruction as a guided flow-matching problem. Flow-matching models define a vector field that establishes a probabilistic path from an initial base distribution to a desired target distribution. By drawing a sample, x_1 , from the base distribution $p_1(x_1)$ and integrating the ordinary differential equation (ODE), $dx_t = v_t(x_t)dt$, we can generate samples x_0 that conform to the target distribution $p_0(x_0)$. We extend this formulation to a guided setting where the target is a conditional distribution, $p_0(x_0|c)$, with c representing the specified contact points on the object’s surface. The objective is to determine a delta velocity vector field, $g_t(x_t)$, such that the updated vector field, $v'_t(x_t) = v_t(x_t) + g_t(x_t)$, directs the probability path from $p_1(x_1)$ toward this conditioned target distribution.

The posterior distribution $p_0(x_0|c)$ can be defined using an energy function $J(x; c)$, such that $p_0(x_0|c) = \frac{1}{Z} p_0(x) e^{-J(x_0; c)}$. The value of $J(x_0; c)$ should be small when x_0 is more compatible with the contact points, and large otherwise. This means that the posterior $p_0(x_0|c)$ is large when x_0 is both realistic and compatible with the contact points. The paper [47] has shown that, under the following assumptions, a valid approximation of the guidance vector field is $g_t(x_t) = \lambda_t \nabla_{x_t} J(\hat{x}_0)$, where $\hat{x}_0 := E_{x_0 \sim p(x_0|x_t)}[x_0]$. The two assumptions are:

- 1) The probability mass of $p(x_0|x_t)$ is centered around its mean.
- 2) The conditional probability path $p_t(x_t|x_0, x_1)$ is affine.

The TRELLIS [26] model uses the affine path $x_t = \alpha_t x_0 + \beta_t x_1$, and the image condition leads to a fairly concentrated $p(x_0|x_t)$. Therefore, these two assumptions are appropriate for our 3D generation model. With the path schedule $\alpha_t = 1 - t$ and $\beta_t = t$, it is straightforward to calculate $\hat{x}_0 = x_t - v_t t$, which is the one-step best prediction of x_0 at time t . The discussion above means that given a contact-induced energy function J , the guidance vector can be calculated by taking the derivative of $J(\hat{x}_0)$ with respect to x_t , together with a properly chosen coefficient λ_t . The resulting guidance is similar to the guidance commonly used in diffusion models, but [47] showed that it is also valid in flow-matching models under the mentioned assumptions. In the following section, we will detail how we design the function J and select the coefficient λ_t .

B. Drag-based Contact Loss

$\hat{x}_0 \in \mathbb{R}^{16 \times 16 \times 16 \times C}$, where C is the channel dimension, is the denoised dense voxel latent for the sparse structure, on which it is hard to measure the compatibility with contact

points. Therefore, we decode the dense voxel latent to the voxel occupancies $\hat{s}_0 = \mathcal{D}(\hat{x}_0) \in \mathbb{R}^{64 \times 64 \times 64}$. \hat{s}_0 can be converted to the sparse structure by binarization, but we use the continuous \hat{s}_0 for guidance. Then we define $J(\hat{x}_0; c) := L(\hat{s}_0; c)$, where L is the contact-induced loss function in the voxel space. \mathcal{D} is a lightweight UNet [60] decoder that is easy to differentiate, which is part of why we choose TRELLIS as our base model. The occupied voxels are a coarse representation of the final geometry. Though lacking some final details, the resolution (64^3) is high enough to apply contact guidance. For example, an object with the largest dimension 30 cm has a quantization error of less than 0.5 cm due to the voxelization.

While it would be straightforward to measure the incompatibility between the sparse voxels and the contact points, for example, by measuring the distance between a contact point and the nearest occupied voxels, such measures cannot be used as the L function because they are not differentiable with respect to \hat{s}_0 . The loss L needs to be a function of the voxel occupancy values. In theory, the loss can be defined to encourage the single voxel right at the contact point to be occupied, but such a loss function is too local to guide the global shape in practice. However, it is an ill-posed problem to define the occupancy loss of a lot of voxels based on a single contact point. Any loss formulation imposes additional biases on the object geometry.

Here is where the drag-based formulation comes into play. Satisfying contact-induced constraints can be viewed as pulling a point on the surface of the object to the contact point, and the contact-based loss L can be formulated similarly to the drag-based loss in the editing task. To obtain a reference to “drag”, we run the unguided flow-matching model once and use the generated voxel occupancy grid $s_0^* \in \mathbb{R}^{64 \times 64 \times 64}$ as the reference. Then, for each contact point p^c , we find the nearest occupied voxel location p^s . The drag-inspired contact loss is defined as:

$$L(\hat{x}_0; p^c) = \sum_{\Delta p \in \mathcal{N}_c} \|\hat{s}_0(p^c + \Delta p) - s_0^*(p^s + \Delta p)\|^2 \quad (1)$$

where \mathcal{N}_c is a 3D neighborhood in the voxel space around the origin. This loss encourages the guided geometry around the contact point to copy the local geometry around the nearest occupied point in the unguided generated shape. In this way, the bias imposed by this occupancy loss is dependent on the input-specific shape prior generated by the model itself. We use this strategy to minimize the bias introduced by manual heuristics. We do not use the content-preservation loss to encourage consistency with the reference occupancy at unguided areas, as in [48], because the input image already provides a strong signal for the 3D generation in the unguided area, which is different from the image editing task.

C. Guidance Scheduling and Attenuation

Now we discuss how to decide λ_t . Principled ways to determine λ_t exist. For example, equation 7 in [47] provides $\lambda_t^{\text{cov-G}} = t/(1-t)$. This is based on approximating the

Algorithm 1 Recurrent guidance (for a single timestep)

- 1: Given current state x_t , denoising transformer \mathcal{T} , energy function J , recurrent step m , guidance weight λ_t , next timestep t_{next}
 - 2: Recurrent step counter $i \leftarrow 0$
 - 3: **while** $i < m$ **do**
 - 4: $v_t \leftarrow \mathcal{T}(x_t)$
 - 5: $\hat{x}_0 \leftarrow x_t - v_t t$
 - 6: $g_t \leftarrow \lambda_t \nabla_{x_t} J(\hat{x}_0)$
 - 7: $x_t \leftarrow x_t + g_t(t_{\text{next}} - t)$
 - 8: $i \leftarrow i + 1$
 - 9: **end while**
 - 10: $x_{t_{\text{next}}} \leftarrow x_t + v_t(t_{\text{next}} - t)$
 - 11: **return** $x_{t_{\text{next}}}$
-

covariance matrix between x_0 and x_t through the Jacobian $\partial \hat{x}_0 / \partial x_t$. However, it has numerical issues near the beginning of denoising ($t \approx 1$) and does not work well in practice in our problem. We empirically found that applying large guidance during the middle stage of the denoising and applying smaller guidance near the beginning and the end works the best. We call this weighting parameter $\lambda_t^{\text{schedule}}$. It coincides with the empirical findings in earlier guided diffusion work [45], but the theoretical analysis is left for future investigation.

We also noticed that the same guidance weight λ_t can have a very different effect when given different input images. In some cases, the guidance barely makes any difference in the denoising process. In some other cases, the guidance corrupts the latent completely and results in failure to finish the generation pipeline. We analyzed the norm of $\nabla_{x_t} J(\hat{x}_0)$, and found that it fluctuates a lot across different input image conditions, and the corruption cases happen when $\|\nabla_{x_t} J(\hat{x}_0)\|$ gets abnormally high. With the chain rule,

$$\nabla_{x_t} J(\hat{x}_0) = \frac{dJ(\hat{x}_0)}{d\hat{x}_0} \frac{d\hat{x}_0}{dx_t} = \nabla_{\hat{x}_0} J(\hat{x}_0) \frac{d\hat{x}_0}{dx_t} \quad (2)$$

$\nabla_{\hat{x}_0} J(\hat{x}_0)$ is dependent on the voxel-space loss function and the voxel occupancy decoder, while $\frac{d\hat{x}_0}{dx_t}$ requires differentiation through the denoising transformer. We found that empirically $\|\nabla_{\hat{x}_0} J(\hat{x}_0)\|$ stays more stable across different image inputs, likely because $\|\nabla_{\hat{x}_0} J(\hat{x}_0)\|$ does not rely on the flow model. Therefore, we applied a guidance attenuation as follows:

$$\lambda_t^{\text{attenuation}} = \frac{\|\nabla_{\hat{x}_0} J(\hat{x}_0)\|}{\|\nabla_{x_t} J(\hat{x}_0)\|} \quad (3)$$

which stabilized the guidance across different inputs and eliminated the failure cases caused by exploding guidance. Overall, we have $\lambda_t = \lambda_t^{\text{schedule}} \lambda_t^{\text{attenuation}}$.

Furthermore, we applied recurrent guidance similar to the self-recurrent guidance in diffusion models [44]. The idea is to apply m steps of guided update before proceeding to the next timestep. It helps the generation adhere to the guidance better without a huge λ , which risks sacrificing the quality. In flow-matching, we implement it following Algorithm 1.

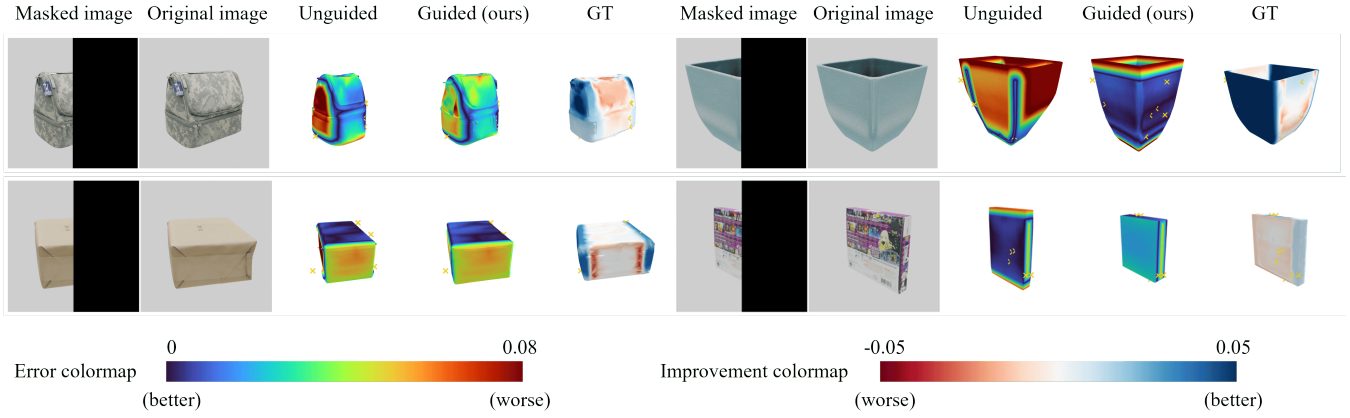


Fig. 2. Qualitative comparison of the geometry reconstruction. The heatmaps on the unguided and guided predictions depict the one-sided point-wise Chamfer distance from the predicted shape (refer to the error colormap). The heatmap on the ground truth (GT) mesh shows the improvement of the one-sided point-wise Chamfer distance from the GT shape (refer to the improvement colormap). The contact points are shown in yellow crossings. They are more visible in Figure 3.

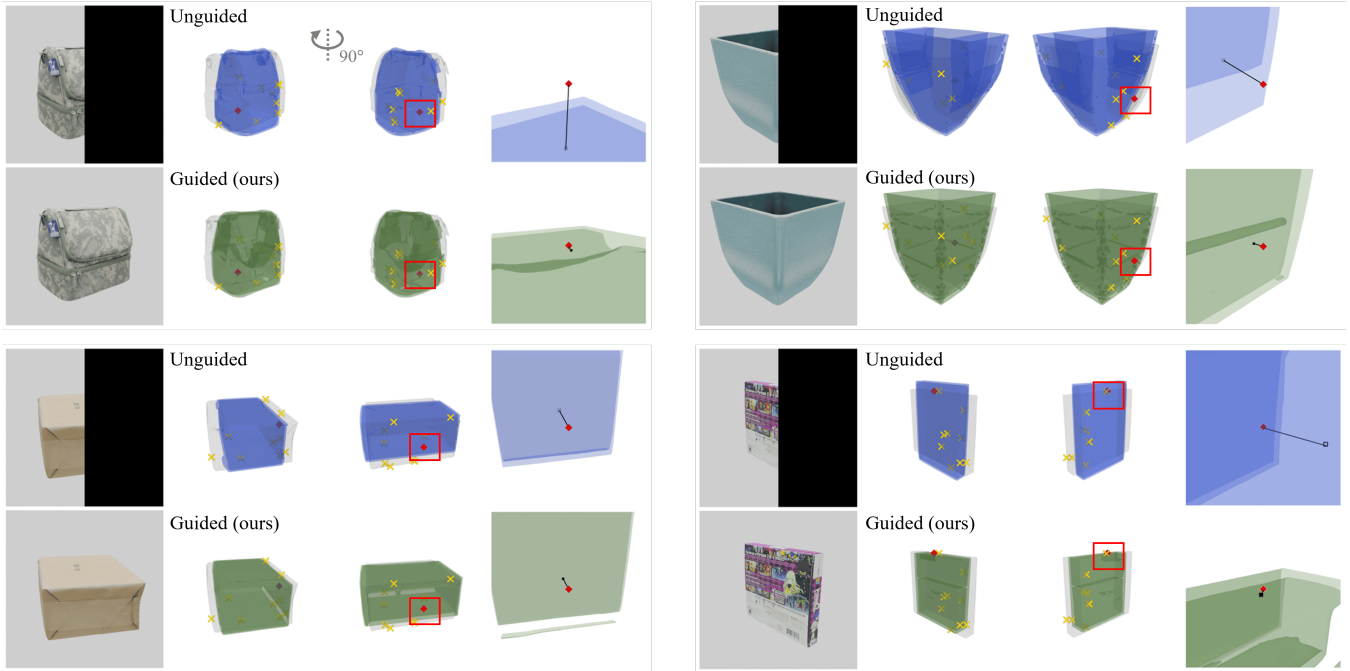


Fig. 3. Qualitative examples of the effect of the contact-point guidance. We show the predicted meshes in two viewing angles, rotated by 90 degrees, for better 3D interpretability. The gray meshes are the ground truth for reference. The red points are the contact points with a zoomed-in visualization on the right (zoomed-in area shown in red square), in which they are connected to the nearest point on the predicted surface, which is shown in black. The yellow crossings are the other 9 contact points.

Methods	Chamfer Distance ↓		F@0.01 ↑		F@0.02 ↑		F@0.05 ↑		RGB-LPIPS ↓	
	Mean	Median	Mean	Median	Mean	Median	Mean	Median	Mean	Median
Unguided Amodal3R [5]	0.0478	0.0425	0.418	0.397	0.621	0.629	0.876	0.914	0.1532	0.1415
Guided w/o recurrence	0.0397	0.0359	0.421	0.398	0.626	0.631	0.882	0.908	0.1529	0.1320
Guided (ours)	0.0385	0.0332	0.426	0.415	0.640	0.653	0.888	0.922	0.1562	0.1374

TABLE I

QUANTITATIVE EVALUATION OF 3D RECONSTRUCTION UNDER OCCLUSION ON THE GSO [61] DATASET. ↓ MEANS SMALLER IS BETTER, ↑ MEANS LARGER IS BETTER. THE BEST IS HIGHLIGHTED IN BOLD FONT. THE OBJECTS ARE NORMALIZED IN A UNIT CUBE.

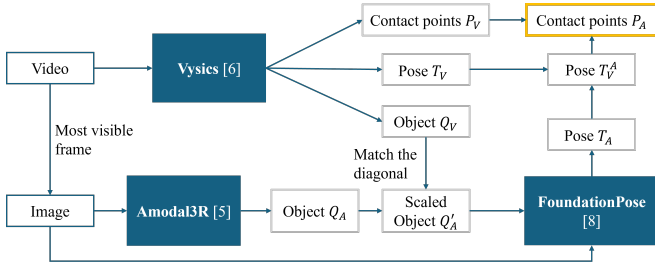


Fig. 4. The process of converting contact points estimated by Vysics to the prediction space of Amodal3R for contact-guidance in real-world experiments. T_V, T_A are the poses of objects Q_V, Q_A in the camera frame. T_V^A converts between the two object frames.

V. EXPERIMENTAL SETUP

A. Shared setup for both experiments

We use the same set of hyperparameters for the experiments on synthetic data and real data. Amodal3R’s [5] flow-matching model has 12 timesteps in total. We split them into early, middle, and late stages, each with 4 timesteps. $\lambda_t^{\text{schedule}}$ is set to 0.2, 1.0, and 0.5, for the early, middle, and late stages, respectively. And we have the recurrent steps $m = 3$ for all timesteps. The 3D neighborhood \mathcal{N}_ϵ for drag-based contact guidance is set to a $21 \times 21 \times 21$ voxel cube.

B. Experiment on synthetic data

The first experiment is the Google Scanned Objects (GSO) [61] dataset. It is a collection of 3D-scanned common household items. We randomly select 200 objects from the dataset and use Blender to render images of the objects, similar to the practice in Amodal3R. Then, we add artificial occlusions to the images simply by masking out the right half of the image. It occludes approximately half of the objects regardless of the object type and pose, and the occlusion mask does not give hints about the object silhouette.

One issue is that 3D generative models like TRELIS [26] are mostly trained on rendered images on which the object is centered, which means that the absolute 2D coordinates of the visible part of an object give hints about the overall size of the object. This is a bias specific to the renderings of 3D object datasets, which is unrealistic for real-world 3D reconstruction under occlusion. Therefore, we add random horizontal shifts to the masked image and feed the collection of shifted images to the network using the multi-diffusion mechanism in TRELIS. The synthetic contact points are generated by randomly sampling 10 points on the object surface, excluding the part that is visible in the occluded image, allowing the contact information to complement the vision modality.

C. Experiment on real-world data

We also conduct experiments on real-world data. Vysics [6] released data on a Franka robot interacting with objects in a tabletop environment. The data includes RGBD videos, in which the objects are partially occluded, the corresponding masks, the robot trajectories, and the ground truth object mesh for evaluation. There are multiple videos of such

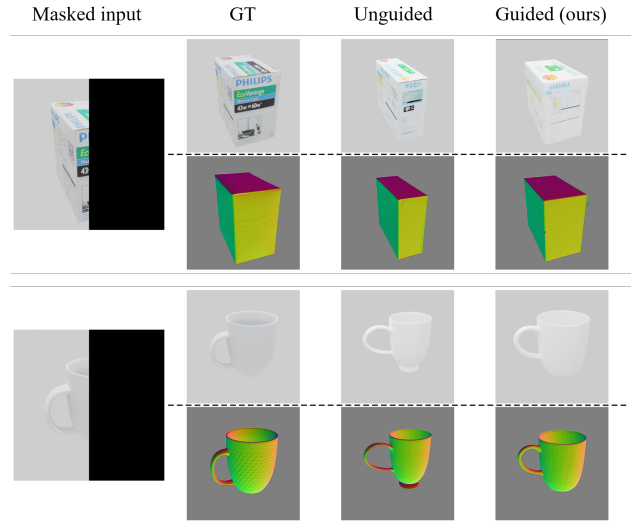


Fig. 5. Examples of the RGB and normal rendering of the ground truth (GT) objects and the generated objects.

interactions for each object, and the inference is on each video independently. We run Vysics on these data and obtain the contact points in Vysic’s object frame. On the other hand, Amodal3R does not work with videos. We select the input image as the frame where the object is most visible based on the area size of the visible object masks. We also crop the image around the visible mask to make the visible part of the object roughly centered and occupy the major part of the image. Note that we don’t have privileged information about the hidden part of the object when cropping the images.

In order to convert the contact points to Amodal3R’s prediction frame, we first run the unguided Amodal3R to obtain an initial reconstructed mesh and align it to the RGBD image using FoundationPose [8]. The scale of the initial mesh is estimated by matching the diagonal length of the best-fitting oriented bounding box between Amodal3R’s predicted mesh and Vysic’s reconstructed mesh using Open3D [62]. Vysics also yields the object’s tracked pose in each RGBD frame. Therefore, the contact points in Vysic’s object frame can be converted to Amodal3R’s object frame. We then run a second run of Amodal3R generation with the guidance of contact points. Vysics typically yields hundreds of contact points that could be redundant for explaining the contact dynamics. We subsample 20 points using farthest point sampling for Amodal3R’s guidance. An overview of this process is depicted in Figure 4.

D. Results on synthetic data

Figure 2 shows examples of the 3D reconstruction under occlusion on the GSO dataset [61], with and without the contact guidance. The heatmaps show that the guided reconstruction has a smaller error to the ground truth shape. To further show the effect of the contact point guidance on the geometry improvement, Figure 3 shows the meshes without texture and with a zoom-in view at one contact point. The distance from the contact point to the nearest point

Categories	bakingbox	bottle	egg	oatly	milk	styrofoam	toblerone	all
BundleSDF [7]	3.84	2.65	3.70	2.45	3.17	2.55	2.44	2.98
Vysics [6]	1.83	1.36	1.05	1.25	1.53	1.45	1.02	1.45
Amodal3R [5]	1.32	1.13	0.52	0.94	1.61	1.90	3.75	1.61
Ours	1.02	1.33	0.50	0.78	1.80	1.95	3.47	1.39

TABLE II

CHAMFER DISTANCE OF THE MESHES RECONSTRUCTED UNDER OCCLUSION ON THE VYSICS [6] REAL-WORLD DATASET. UNIT: CM.

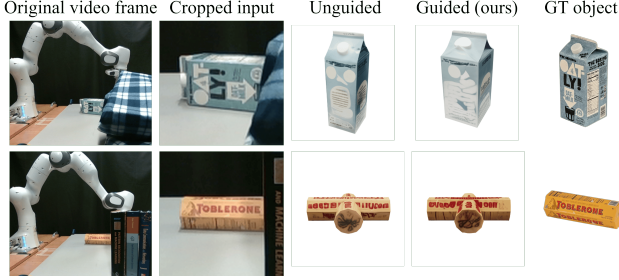


Fig. 6. Qualitative examples of 3D reconstruction on Vysics data. The top row is a successful case, and the bottom row is a failure case.

is reduced after the guidance. The quantitative results are shown in Table I. In terms of the 3D evaluation, we measure the Chamfer distance and the F-score of the points on the predicted shape at different distance thresholds. We also report the LPIPS score [63] of the rendered RGB images, in order to evaluate the quality of the generated objects. The contact-guided generation outperforms the baseline, unguided Amodal3R generation, consistently across the 3D metrics, while maintaining comparable quality in terms of the LPIPS score. We also show the quality of the generated shapes through RGB and normal renderings in Figure 5. The ablation comparison in terms of the recurrent guidance strategy is also shown in Table I. The contact guidance is less effective without the recurrent steps.

E. Results on real-world data

Table II shows the quantitative results of the 3D reconstruction under occlusion in the real-world data provided by Vysics [6]. The comparisons include BundleSDF [7], representing pure vision-based reconstruction; Vysics [6], representing joint optimization of vision and physics-based reasoning; Amodal3R [5], representing visual reconstruction with generative prior knowledge; and ours, which combines vision, generative priors, and physics-based insights of the contacts. Our method achieved the overall best geometric accuracy in terms of Chamfer distance. Specifically, our method tends to improve further when Amodal3R provides a reasonable unguided generation, but does not help as much when the initial result is far off. See Figure 6 as an example. In the first row (oatly), the unguided generation has the correct structure but the wrong aspect ratio. The contact-point guidance can help fix it. In the second row (toblerone), the initial generation has the wrong shape overall, and the guidance couldn’t recover from such an error.

VI. CONCLUSIONS

Our work still has limitations. From the qualitative examples, we can see that the guided generation may still not satisfy the contact-induced constraints exactly, though moving in the correct direction. The drag-based guidance loss assumes that the unguided results have roughly correct structure, which may not be the case in practice. We will explore solutions to these problems in future work.

In summary, we explored the integration of data-driven 3D shape priors and physics-driven contact information to tackle the challenging task of 3D object reconstruction under heavy occlusion, in the form of guided flow-matching generation. We propose a drag-based contact loss function to guide the dense voxel map with sparse contact points while introducing minimal heuristic bias. Experimental results on synthetic data and real-world data both show that our framework improves the reconstruction accuracy by incorporating both sources of knowledge. We hope this work could inspire more explorations of joining the merits of big data and physics-based insights for building more powerful robot vision systems.

ACKNOWLEDGMENT

This work was supported by an NSF CAREER Award under Grant No. FRR-2238480 and the RAI Institute. M. Ghaffari was supported by AFOSR MURI FA9550-23-1-0400 and AFOSR YIP FA9550-25-1-0224.

REFERENCES

- [1] T. Pang et al., “Global planning for contact-rich manipulation via local smoothing of quasi-dynamic contact models,” *IEEE Transactions on robotics*, vol. 39, no. 6, pp. 4691–4711, 2023.
- [2] S. Venkatesh et al., “Approximating global contact-implicit mpc via sampling and local complementarity,” *arXiv preprint arXiv:2505.13350*, 2025.
- [3] C. Chi et al., “Diffusion policy: Visuomotor policy learning via action diffusion,” *The International Journal of Robotics Research*, p. 02783649241273668, 2023.
- [4] A. Brohan et al., “Rt-1: Robotics transformer for real-world control at scale,” *arXiv preprint arXiv:2212.06817*, 2022.
- [5] T. Wu et al., “Amodal3R: Amodal 3D Reconstruction from Occluded 2D Images,” *arXiv preprint arXiv:2503.13439*, 2025.
- [6] B. Bianchini et al., “Vysics: Object reconstruction under occlusion by fusing vision and contact-rich physics,” in *Robotics: Science and Systems (RSS)*, 2025.
- [7] B. Wen et al., “Bundlesdf: Neural 6-dof tracking and 3d reconstruction of unknown objects,” in *Proceedings of the IEEE/CVF Conference on Computer Vision and Pattern Recognition*, 2023, pp. 606–617.
- [8] B. Wen et al., “Foundationpose: Unified 6d pose estimation and tracking of novel objects,” in *Proceedings of the IEEE/CVF Conference on Computer Vision and Pattern Recognition*, 2024, pp. 17868–17879.
- [9] R. Rombach et al., “High-resolution image synthesis with latent diffusion models,” in *Proceedings of the IEEE/CVF Conference on Computer Vision and Pattern Recognition*, 2022, pp. 10684–10695.
- [10] S. Szymanowicz et al., “Viewset diffusion: (0-)image-conditioned 3d generative models from 2d data,” in *Proceedings of the IEEE/CVF international conference on computer vision*, 2023, pp. 8863–8873.
- [11] Y. Xu et al., “Dmv3d: Denoising multi-view diffusion using 3d large reconstruction model,” in *The Twelfth International Conference on Learning Representations*, 2024.
- [12] B. Poole et al., “Dreamfusion: Text-to-3d using 2d diffusion,” in *The Eleventh International Conference on Learning Representations*, 2023.
- [13] R. Liu et al., “Zero-1-to-3: Zero-shot One Image to 3D Object,” in *Proceedings of the IEEE/CVF international conference on computer vision*, 2023, pp. 9298–9309.

- [14] P. Wang et al., "Imagedream: Image-prompt multi-view diffusion for 3d generation," *arXiv preprint arXiv:2312.02201*, 2023.
- [15] M. Liu et al., "One-2-3-45: Any single image to 3d mesh in 45 seconds without per-shape optimization," *Advances in Neural Information Processing Systems*, vol. 36, pp. 22 226–22 246, 2023.
- [16] J. Li et al., "Instant3d: Fast text-to-3d with sparse-view generation and large reconstruction model," in *The Twelfth International Conference on Learning Representations*, 2024.
- [17] X. Long et al., "Wonder3d: Single image to 3d using cross-domain diffusion," in *Proceedings of the IEEE/CVF conference on computer vision and pattern recognition*, 2024, pp. 9970–9980.
- [18] C. Lin et al., "DiffSplat: Repurposing Image Diffusion Models for Scalable Gaussian Splat Generation," in *The Thirteenth International Conference on Learning Representations*, 2025.
- [19] P. Mittal et al., "AutoSDF: Shape Priors for 3D Completion, Reconstruction and Generation," in *Proceedings of the IEEE/CVF conference on computer vision and pattern recognition*, 2022, pp. 306–315.
- [20] Y.-C. Cheng et al., "SDFusion: Multimodal 3D Shape Completion, Reconstruction, and Generation," in *Proceedings of the IEEE/CVF conference on computer vision and pattern recognition*, 2023, pp. 4456–4465.
- [21] A. X. Chang et al., "Shapenet: An information-rich 3d model repository," *arXiv preprint arXiv:1512.03012*, 2015.
- [22] M. Deitke et al., "Objaverse: A universe of annotated 3d objects," in *Proceedings of the IEEE/CVF conference on computer vision and pattern recognition*, 2023, pp. 13 142–13 153.
- [23] L. Zhang et al., "Clay: A controllable large-scale generative model for creating high-quality 3d assets," *ACM Transactions on Graphics (TOG)*, vol. 43, no. 4, pp. 1–20, 2024.
- [24] B. Zhang et al., "3DShape2VecSet: A 3D Shape Representation for Neural Fields and Generative Diffusion Models," *ACM Transactions On Graphics (TOG)*, vol. 42, no. 4, pp. 1–16, 2023.
- [25] Z. Zhao et al., *Hunyuan3D 2.0: Scaling Diffusion Models for High Resolution Textured 3D Assets Generation*, 2025.
- [26] J. Xiang et al., "Structured 3D Latents for Scalable and Versatile 3D Generation," in *Proceedings of the Computer Vision and Pattern Recognition Conference*, 2025, pp. 21 469–21 480.
- [27] Z. Chen et al., "3dtopia-xl: Scaling high-quality 3d asset generation via primitive diffusion," in *Proceedings of the Computer Vision and Pattern Recognition Conference*, 2025, pp. 26 576–26 586.
- [28] L. Yushi et al., "Gaussiananything: Interactive point cloud flow matching for 3d object generation," in *The Thirteenth International Conference on Learning Representations*, 2025.
- [29] E. Ozguroglu et al., "Pix2gestalt: Amodal Segmentation by Synthesizing Wholes," in *Proceedings of the IEEE/CVF conference on computer vision and pattern recognition*, 2024, pp. 3931–3940.
- [30] K. Chen et al., "Using Diffusion Priors for Video Amodal Segmentation," in *Proceedings of the Computer Vision and Pattern Recognition Conference*, 2025, pp. 22 890–22 900.
- [31] S. Xie et al., "Smartbrush: Text and shape guided object inpainting with diffusion model," in *Proceedings of the IEEE/CVF conference on computer vision and pattern recognition*, 2023, pp. 22 428–22 437.
- [32] A. Lugmayr et al., "Repaint: Inpainting using denoising diffusion probabilistic models," in *Proceedings of the IEEE/CVF Conference on Computer Vision and Pattern Recognition*, 2022, pp. 11 461–11 471.
- [33] A. Agarwal et al., "SceneComplete: Open-World 3D Scene Completion in Complex Real World Environments for Robot Manipulation," *arXiv preprint arXiv:2410.23643*, 2024.
- [34] X. Ju et al., "BrushNet: A Plug-and-Play Image Inpainting Model with Decomposed Dual-Branch Diffusion," in *European Conference on Computer Vision*, Springer, 2024, pp. 150–168.
- [35] J. Xu et al., "Instantmesh: Efficient 3d mesh generation from a single image with sparse-view large reconstruction models," *arXiv preprint arXiv:2404.07191*, 2024.
- [36] K. Yao et al., "Cast: Component-aligned 3d scene reconstruction from an rgb image," *ACM Transactions on Graphics (TOG)*, vol. 44, no. 4, pp. 1–19, 2025.
- [37] M. Oquab et al., "Dinov2: Learning robust visual features without supervision," *Transactions on Machine Learning Research Journal*, 2024.
- [38] G. Chou et al., "Diffusion-SDF: Conditional Generative Modeling of Signed Distance Functions," in *Proceedings of the IEEE/CVF international conference on computer vision*, 2023, pp. 2262–2272.
- [39] W. Yuan et al., "Pcn: Point completion network," in *2018 international conference on 3D vision (3DV)*, IEEE, 2018, pp. 728–737.
- [40] X. Yu et al., "Pointtr: Diverse point cloud completion with geometry-aware transformers," in *Proceedings of the IEEE/CVF international conference on computer vision*, 2021, pp. 12 498–12 507.
- [41] Z. Chen et al., "Anchorformer: Point cloud completion from discriminative nodes," in *Proceedings of the IEEE/CVF conference on computer vision and pattern recognition*, 2023, pp. 13 581–13 590.
- [42] L. Zhang et al., "Adding conditional control to text-to-image diffusion models," in *Proceedings of the IEEE/CVF international conference on computer vision*, 2023, pp. 3836–3847.
- [43] C. Mou et al., "T2i-adapter: Learning adapters to dig out more controllable ability for text-to-image diffusion models," in *Proceedings of the AAAI conference on artificial intelligence*, vol. 38, 2024, pp. 4296–4304.
- [44] A. Bansal et al., "Universal guidance for diffusion models," in *Proceedings of the IEEE/CVF conference on computer vision and pattern recognition*, 2023, pp. 843–852.
- [45] J. Yu et al., "Freedom: Training-free energy-guided conditional diffusion model," in *Proceedings of the IEEE/CVF International Conference on Computer Vision*, 2023, pp. 23 174–23 184.
- [46] H. Chung et al., "Diffusion posterior sampling for general noisy inverse problems," *The Eleventh International Conference on Learning Representations, ICLR 2023*, 2023.
- [47] R. Feng et al., "On the guidance of flow matching," *Forty-second International Conference on Machine Learning*, 2025.
- [48] C. Mou et al., "Dragondiffusion: Enabling drag-style manipulation on diffusion models," *arXiv preprint arXiv:2307.02421*, 2023.
- [49] Y. Shi et al., "Dragdiffusion: Harnessing diffusion models for interactive point-based image editing," in *Proceedings of the IEEE/CVF Conference on Computer Vision and Pattern Recognition*, 2024, pp. 8839–8849.
- [50] W. Agnew et al., "Amodal 3d reconstruction for robotic manipulation via stability and connectivity," in *Conference on robot learning*, PMLR, 2021, pp. 1498–1508.
- [51] J. Ni et al., "Phyrecon: Physically plausible neural scene reconstruction," *Advances in Neural Information Processing Systems*, vol. 37, pp. 25 747–25 780, 2024.
- [52] K. Yao et al., "Cast: Component-aligned 3d scene reconstruction from an rgb image," *ACM Transactions on Graphics (TOG)*, vol. 44, no. 4, pp. 1–19, 2025.
- [53] W. Yang et al., "Twintrack: Bridging vision and contact physics for real-time tracking of unknown dynamic objects," *arXiv preprint arXiv:2505.22882*, 2025.
- [54] C. Song et al., "Inferring 3d shapes of unknown rigid objects in clutter through inverse physics reasoning," *IEEE robotics and automation letters*, vol. 4, no. 2, pp. 201–208, 2018.
- [55] B. Chen et al., "Physgen3d: Crafting a miniature interactive world from a single image," in *Proceedings of the Computer Vision and Pattern Recognition Conference*, 2025, pp. 6178–6189.
- [56] H. Jiang et al., "Phystwin: Physics-informed reconstruction and simulation of deformable objects from videos," *IEEE International Conference on Computer Vision (ICCV)*, 2025.
- [57] T. Shen et al., "Flexible isosurface extraction for gradient-based mesh optimization," *ACM Transactions on Graphics (TOG)*, vol. 42, no. 4, pp. 1–16, 2023.
- [58] X. Pan et al., "Drag your gan: Interactive point-based manipulation on the generative image manifold," in *ACM SIGGRAPH 2023 conference proceedings*, 2023, pp. 1–11.
- [59] H. Chen et al., "Mvdrag3d: Drag-based creative 3d editing via multi-view generation-reconstruction priors," *arXiv preprint arXiv:2410.16272*, 2024.
- [60] O. Ronneberger et al., "U-net: Convolutional networks for biomedical image segmentation," in *International Conference on Medical Image Computing and Computer-assisted Intervention*, Springer, 2015, pp. 234–241.
- [61] L. Downs et al., "Google scanned objects: A high-quality dataset of 3d scanned household items," in *2022 International Conference on Robotics and Automation (ICRA)*, IEEE, 2022, pp. 2553–2560.
- [62] Q.-Y. Zhou et al., "Open3d: A modern library for 3d data processing," *arXiv preprint arXiv:1801.09847*, 2018.
- [63] R. Zhang et al., "The unreasonable effectiveness of deep features as a perceptual metric," in *Proceedings of the IEEE conference on computer vision and pattern recognition*, 2018, pp. 586–595.